Rheological inheritance controls the formation of segmented rifted margins in cratonic lithosphere

M. Gouiza[1]* and J. Naliboff[2,3]

[1] School of Earth and Environment, University of Leeds, Leeds, UK.

[2] Department of Earth and Planetary Sciences, University of California, Davis, USA.

[3] New Mexico Institute of Mining and Technology, Socorro, New Mexico, USA.

*email: m.gouiza@leeds.ac.uk

Observations from rifted margins reveal that significant structural and crustal heterogeneity develops through the process of continental extension and breakup. While a clear link exists between distinct margin structural domains and specific phases of rifting, the origin of strong segmentation along the length of margins remains relatively enigmatic and may reflect multiple competing factors. Given that rifting frequently initiates on complex tectonics sutures, structural inheritance is frequently invoked as an origin of margin segmentation, although to date no studies have clearly elucidated the link between inheritance and 3D rifted margin geometries. Here, we use recent observations from the Labrador Sea and thermal-mechanical simulations of continental rifting to constrain the effects of inherited variable lithospheric properties on margin segmentation. The modelling results demonstrate that N-S variations in lithospheric thickness, crustal structure, and rheology within the pre-rift Canadian Shield produce sharp gradients in rifted margin width and the timing of breakup, leading to strong margin segmentation across a range of geophysically-constrained rift parameters.

The formation of rifted continental margins occurs through multiple phases of extension with distinct structural, sedimentary, and magmatic characteristics[1,2]. A synthesis of key features at Atlantic rifted margins[2] suggests that most rifted margins undergo a similar sequence of deformation phases, which reflect progressive thinning of the continental lithosphere that produces a transition from distributed to highly localized deformation.

While this sequence produces genetically similar 'domains' from the un-rifted continent to the seafloor, significant heterogeneity still exists between distinct rifted margins[2] and along the length of individual rifted margins that are characterized by distinct segments. As most rift basins form along (or near) former orogens[3], pre-existing structures and associated variations are commonly invoked to explain the segmentation of both rifts and rifted margins.

Numerical modelling supports this inferred link between pre-rift structure and rifted margin architecture, with a wide range of 2D investigations demonstrating the first-order effects of the initial thermal and rheological structure on continental rifting[4–9]. 2D modelling also suggests that extension velocity[7–9], multiphase rifting[10], and complex deformation network localization [11–13] exert a first-order control on rifted margin structure. Furthermore, 3D numerical simulations can now achieve similar spatial resolutions to 2D studies and illustrate the margin-parallel effects of both structural inheritance[14–17], fault network coalescence[18] and out-of-plane[19] or oblique[20,21] boundary conditions.

Despite these advances, to date no studies have explicitly examined the effects of variable lithospheric structure on the 3D evolution of continental rifting and rifted margin segmentation. This in part reflects

that the many rifted margins initiate on complex pre-rift lithosphere[3], which may be difficult to accurately reconstruct and include short-wavelength structural variations (i.e., brittle faults, ductile shear zones) whose relationship to extensional structures is often difficult to constrain without high-resolution seismic data to connect onshore and offshore structures[22].

An exception to this is the Labrador Sea between Greenland and Canada, which formed through rifting of a cratonic lithosphere that exhibits clearly defined N-S variations in crustal and lithospheric thickness and composition[23–25]. Here, we use recent observations from the Labrador Sea rifted margin[26] and thermal-mechanical modelling to examine the effects of variations in pre-rift lithospheric structure on rift evolution and margin architecture. The numerical design and assessment is directly informed by a wide range of geologic and geophysical constraints on pre-rift and syn-rift evolution, which we first outline in detail (see also Supplementary Notes 1-3). Our investigation reveals that variations in cratonic lithosphere structure and composition can reproduce key first-order observations of rifted margin crustal architecture in the Labrador Sea.

Rifting and segmentation of the Labrador Sea

The Labrador Sea formed between E Canada and SW Greenland as a branch of the North Atlantic Ocean[27]. Rifting in the early to Late Cretaceous produced large-offset deformation structures and sedimentary packages in the necking and distal domain, which initiated on Archean to Proterozoic terranes amalgamated during the late Mesoproterozoic Grenvillian orogenic collision (ca. 10.8-0.97 Ga)[26]. Recent studies revealed important changes in rift geometry, crustal architecture, timing and nature of breakup along the Labrador margin[26,28,29]. These changes occur across major Precambrian structures, which run perpendicular to the main NW rift trend and define three margin segments (Fig. 1). The southern segment initiated on Mesoproterozoic basement and shows a typical wide magma-poor rifted margin architecture with hyperextended continental crust and exhumed mantle. The central segment initiated on Palaeoproterozoic basement and also contains domains of hyperextended crust and exhumed mantle, but consists of volcanics in the continent-ocean transition not observed in the south. The northern segment, which initiated on Archean terranes, displays a narrow magma-rich margin architecture with thick packages of seaward-dipping flood basalts and magmatic underplating (Fig. 1). Magnetic[30] and seismic[26] data indicate a diachronous continental breakup younging northward, with ca. 8 Myr gap between the onset of oceanic accretion in the southern segment and the northern segment (Supplementary Note 1). In the latter, breakup appears to coincide with Iceland-plume-related flood basalts (ca. 61–56 Ma) located near the Davis Strait[31]. However, estimated extension rates along the Labrador margin suggest a southward increase in rifting velocities from about 1 mm/yr in the northern segment to 1.6 to 2.6 mm/yr in the central segment and reaching 3 to 4.3 mm/yr in the southern segment (Fig. 1, Supplementary Note 1 and Supplementary Table 1).

Geophysical data collected onshore (i.e. Canadian Shield) and offshore the Labrador Sea reveal the existence of variable heterogeneity in the unrifted lithosphere of the distinct margin segments[23–25,32]. While the continental crust appears to thin northward (i.e., from ~50 km in the southern segment to ~35 km in the central segment[25,32]), the lithosphere thins (i.e., from 250–200 km in the northern segment to 200–150 km in the southern segment[23,24]) and becomes hotter and more depleted[23] southward. The southward lithosphere thinning is consistent with the southward increase in surface heat flow within the Canadian Shield[33].

To examine the effects of these observed variations in lithospheric thickness, composition, and thermal structure on rift segmentation and margin architecture, we have developed thermo-mechanical models that assimilate the unique onshore geophysical constraints for each domain (Fig. 2). While the observations sufficiently constrain first-order variations in crustal and lithospheric thickness (Supplementary Note 2), the rheology of distinct

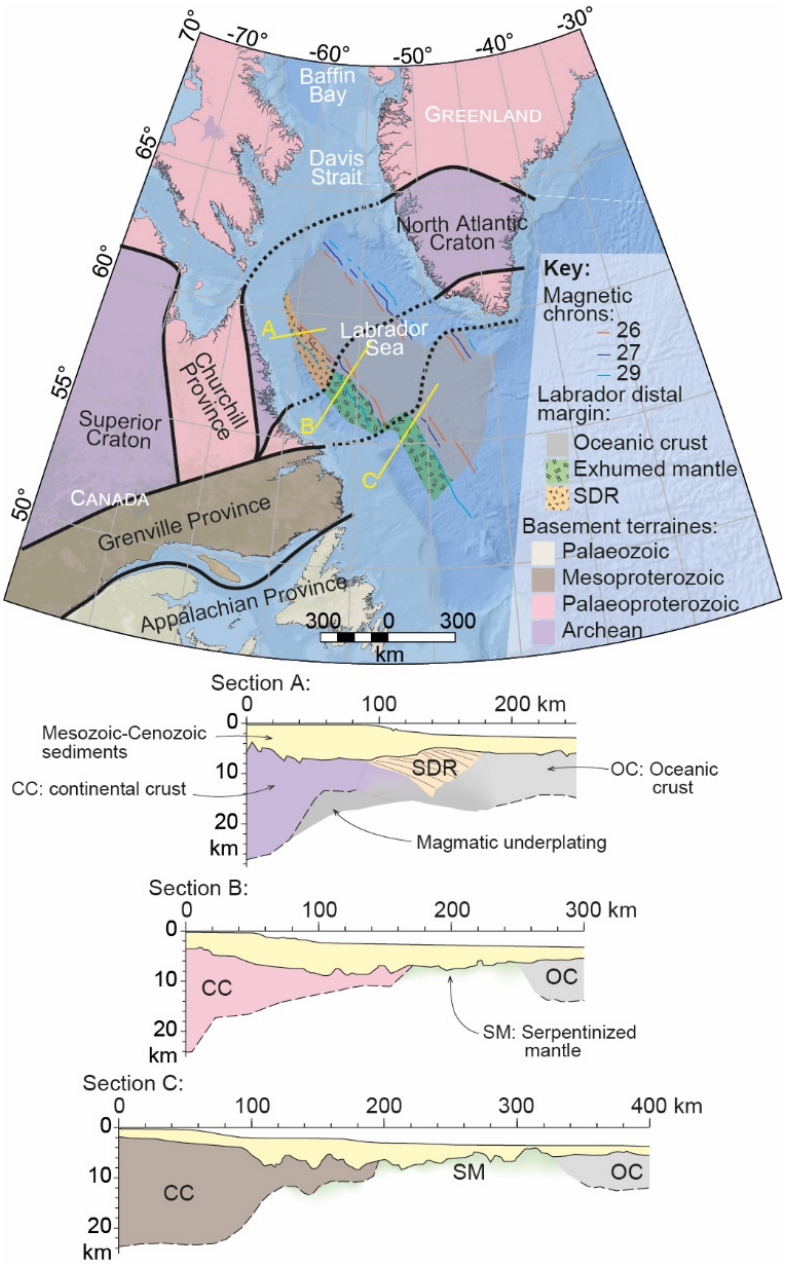

Fig. 1 | Geologic overview of the Labrador Sea and the surrounding unrifted cratonic domains. Map of the Labrador Sea showing the rifted margins[26] and the Archean-Proterozoic cratonic basement onshore East Canada and South Greenland[33]. Cross-sections A to C illustrate the crustal architecture in the northern, central, and southern segments of the Labrador margin[26], respectively.

crustal layers is largely unknown. Consequently, a robust sensitivity analysis is necessary to account for the uncertainties in both crustal rheological layering and rates of extension. Given the extensive computational requirements of high-resolution 3D simulations, our analysis uses a combination of 2D and 3D models, with the 2D models constructed to represent the southern, central, or northern margin segments. We conduct the numerical experiments using the open-source finite element code ASPECT (v2.1.0-pre)34,35, which is capable of efficiently solving for highly non-linear 3D lithospheric deformation. The full results of the sensitivity analysis (Supplementary Videos 1 to 18) and model parameters (Supplementary Table 2) are presented in the Supplementary Information.

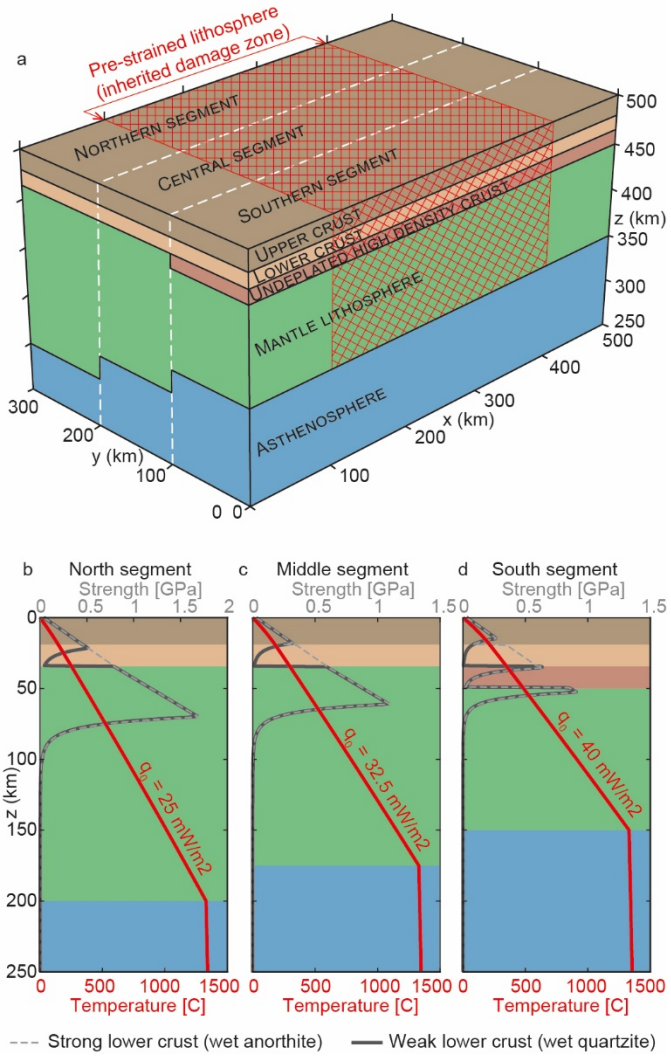

Fig. 2 | Initial setup of the numerical experiments. (a) The numerical experiments assume an initial lithosphere that is 200 km thick in the northern segment, 175 km thick in the central segment, and 150 km thick in the southern segment. The crust in the north and centre is 35 km thick and made of a 20 km thick upper crust and 15 km thick lower crust. In the south, the crust is 50 km thick and made of a 20 km thick upper crust, a 15 km thick lower crust, and a 15 km thick underplated crust. To localise deformation, a pre-strained zone consisting of both plastic and viscous strain is implemented in all models, which is 300 km wide and stretches down to the LAB (lithosphere-asthenosphere boundary). The initial plastic and viscous strain is randomized between values of 0.5-1.5, and both the brittle (cohesion, angle of internal friction) and viscous (pre-yield viscosity) strength are linearly weakened by a factor of 4 over this range. (b-d) The initial geothermal gradient (red line) is uniform within each segment but increases southward between the segments and is calculated assuming surface heat flows observed in the Canadian Shield (q_0) and a constant LAB temperature at 1330 °C (see detailed description of initial thermal structure and thermal parameters in Supplementary Note 3 and Supplementary Table 1) . The initial strength of the lithosphere depends on the composition of the lower crust, which is governed either by wet quartzite[36] (solid grey line) or wet anorthite[37] (dashed grey line) creep laws.

Cratonic structure controls the timing and style of breakup

To assess the interplay between rheology and extension rate in each margin segment, we ran 2D numerical experiments of slow (5 mm/yr) and fast (10 mm/yr) lithospheric extension with either an entirely weak crust (wet quartzite[38], Figure 3a-h) or a weak upper crust and a strong (wet anorthite[37]) lower crust (Fig. 3i-p). Here, we focus on the end-member

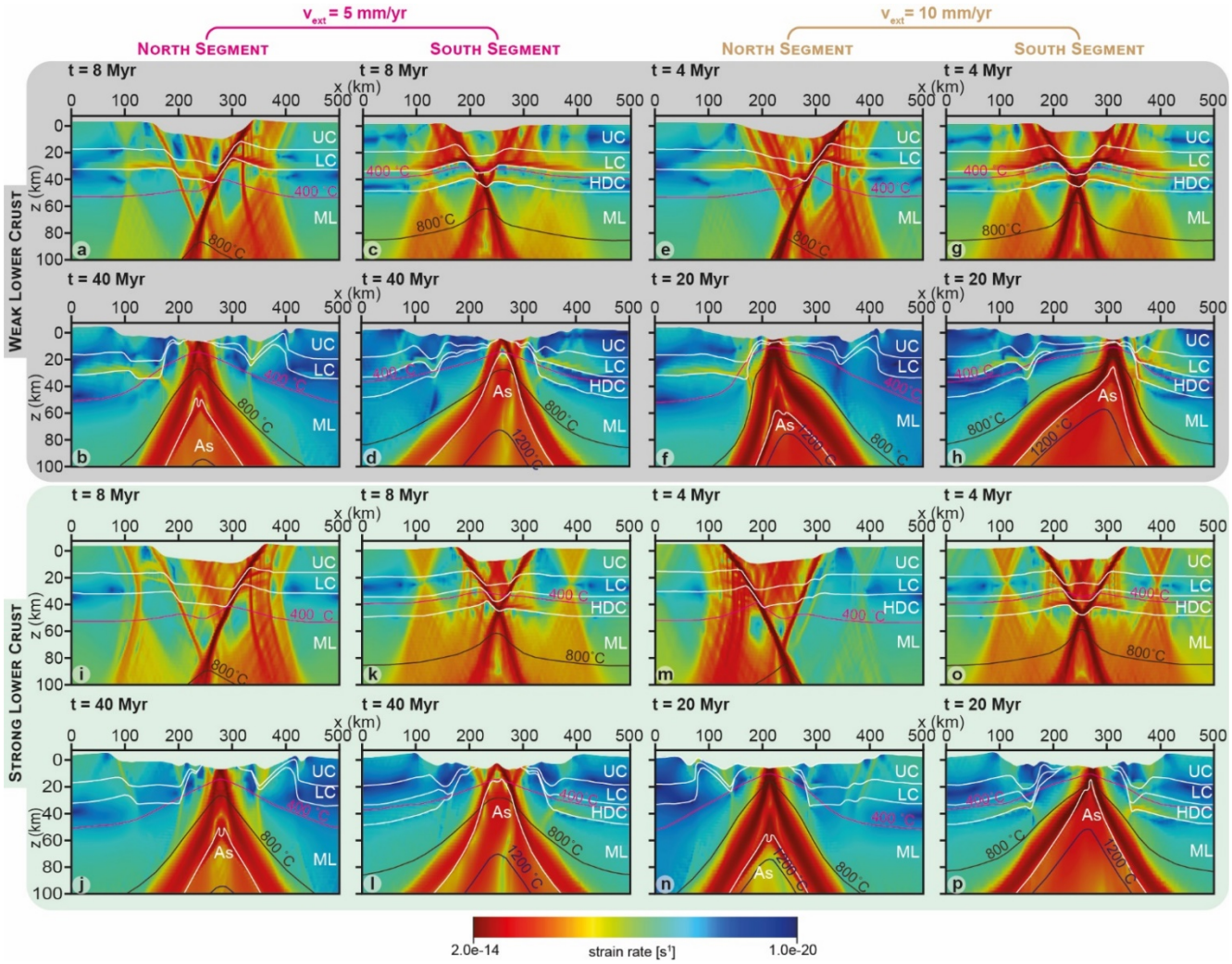

Fig. 3 | 2D modelling results. 2D numerical simulations at selected time steps, which illustrate the early stretching phase and the crustal breakup phase. Models with a weak lower crust (a-h) show an initial pure shear stretching, followed by simple shear extension that results in an asymmetric crust geometry at crustal breakup. Models with a strong lower crust (i-p) show a stretching process dominated by pure shear, which leads to a symmetrical crust geometry at breakup. Increasing the extension rate (v_{ext}) from 5 mm/yr (a-d, i-l) to 10 mm/yr (e-h, m-p) increases the amount of strain required to achieve breakup but has little impact on the architecture of the rifted margins. Shown are strain rate (in jet colour map), isotherms at 400 (pink line), 800 (dark brown line), 1200 °C (dark blue line), and material boundaries (white lines; UC: upper crust; LC: lower crust; HDC: underplated high density crust; ML: mantle lithosphere; As: asthenosphere).

northern and southern segments. In all models, the lithosphere undergoes a three-stage rift evolution with a short-lived distributed stretching phase, followed by a localized necking phase, and finally a breakup phase (Fig. 3, Supplementary Videos 1 to 12). When the lower crust is weak (Fig. 3a-h, Supplementary Videos 1-3 and 7-9), the initial lithospheric stretching duration is governed by a variable crustal ductile layer thickness(es), which increases southward as the geothermal gradient and crustal thickness increase (Fig. 2b-d). Once ductile flow in the upper lithosphere becomes negligible and coupling occurs between the brittle lithospheric layers, deformation localises along a lithospheric-scale shear zone and ensuing rapid thinning leads to the necking of the lithosphere. Early during the necking stage, extension switches from pure to simple shear mode and results in the asymmetric hyperextension of the crust, crustal breakup, mantle exhumation, and finally full lithospheric breakup (Fig. 3a-h). Consistent with previous studies, increasing velocity, higher geothermal gradient, and thicker crust promote a

longer phase of hyperextension and thus a wider zone of hyperextended crust in the final rift configuration.

In the case of a strong lower crust (Fig. 3i-p, Supplementary Videos 4-6 and 10-12), ductile layers within the crust (Fig 2b) are absent and deformation initiates in a coupled manner (Fig. 3i,k,m,o). In both the north (Fig. 3i,m) and south (Fig. 3k,o), the stronger crust suppresses the hyperextension phase and crust breakup occurs both earlier (less total strain) and in a symmetric manner. Prior to the full lithospheric breakup, the sub-continental mantle is exposed, and simple shear appears to dominate the final thinning of the mantle lithosphere (Fig. 3j,l,n,p). In contrast to the weak crust scenario (Fig. 3b,d,f,h), the extension rate, geothermal gradient and crustal thickness have significantly less impact on the final crustal architecture (Fig. 3j,l,n,p)

These results support the hypothesis that observed crustal architecture variability along the Labrador margin is related to initial variation in geothermal gradient, thickness and composition of the crust and the lithosphere. Furthermore, the results suggest that the initial lower crust was stronger in the north than in the south, which in combination with variations in the geothermal gradient enabled north-south gradients in the degree of hyperextension and margin asymmetry. However, the lack of margin-parallel deformation in the 2D simulations could also neglect a process that produces margin segmentation without invoking a north-south change in crustal rheology. To test this finding, we conducted a suite of 3D simulations (Figure 4, Supplementary Videos 13-18) that encompass the physical parameters examined with the 2D simulations.

Lateral rheological heterogeneities promote margin segmentation

Composition and temperature jointly control the rheology and strength of the lithosphere. In cratonic domains, the poly-phase geodynamic evolution and amalgamation of different tectonic terranes result in lateral rheological heterogeneities[39,40]. Our 3D models capture this lateral variability by including the three tectonic domains (Fig. 2), which are defined by variations in the geothermal gradient, crustal and lithospheric structure.

Following the 2D model results (Fig. 3), we conducted four 3D simulations with either a strong or a weak lower crust and an extension rate of 5 or 10 mm/yr (Supplementary Videos 13-16). For these scenarios, minimal margin segmentation and variations in the timing of breakup occur. However, imposing a strong lower crust in the north segment and a weak lower crust in the central and south segments leads to significant margin segmentation for an extension velocity of either 5 or 10 mm/yr (Fig 4., Supplementary Videos 17 and 18). As such, these simulations provide the best fit to the observations of margin segmentation (Fig. 1 and 4).

The temporal evolution (Fig. 4a-b) reveals that structural segmentation occurs early on in the stretching process as primary shear zones develop across the entire model crosscutting the rheological boundaries. Concurrently, secondary shear zones remain restricted to certain segments and either terminate or coalesce near segment boundaries (Fig. 4).

The segmentation between the southern, central, and northern segments becomes more pronounced once the necking phase initiates. In the northern segment where the lithosphere is cold and strong, deformation is coupled at the start of rifting and crustal necking leads to the complete thinning of the crust. Whereas in the southern segment, where the lithosphere is hotter and weaker and the crust is thicker, coupling is delayed and crustal necking leads to a prolonged phase of hyperextension. As a result, crustal breakup starts in the north and propagates southward.

However, lithospheric breakup initiates in the south, where the initial mantle lithosphere is thinner, and propagates northward. The breakup process spreads over 18 Myr for the crust and 6 Myr for the mantle lithosphere. The margin architecture at breakup shows a pronounced crustal segmentation between the three tectonic domains, with a crustal geometry that is narrow in the north and widens southward (Fig. 4d-e). The change in rift evolution and crustal architecture produced by the model are consistent

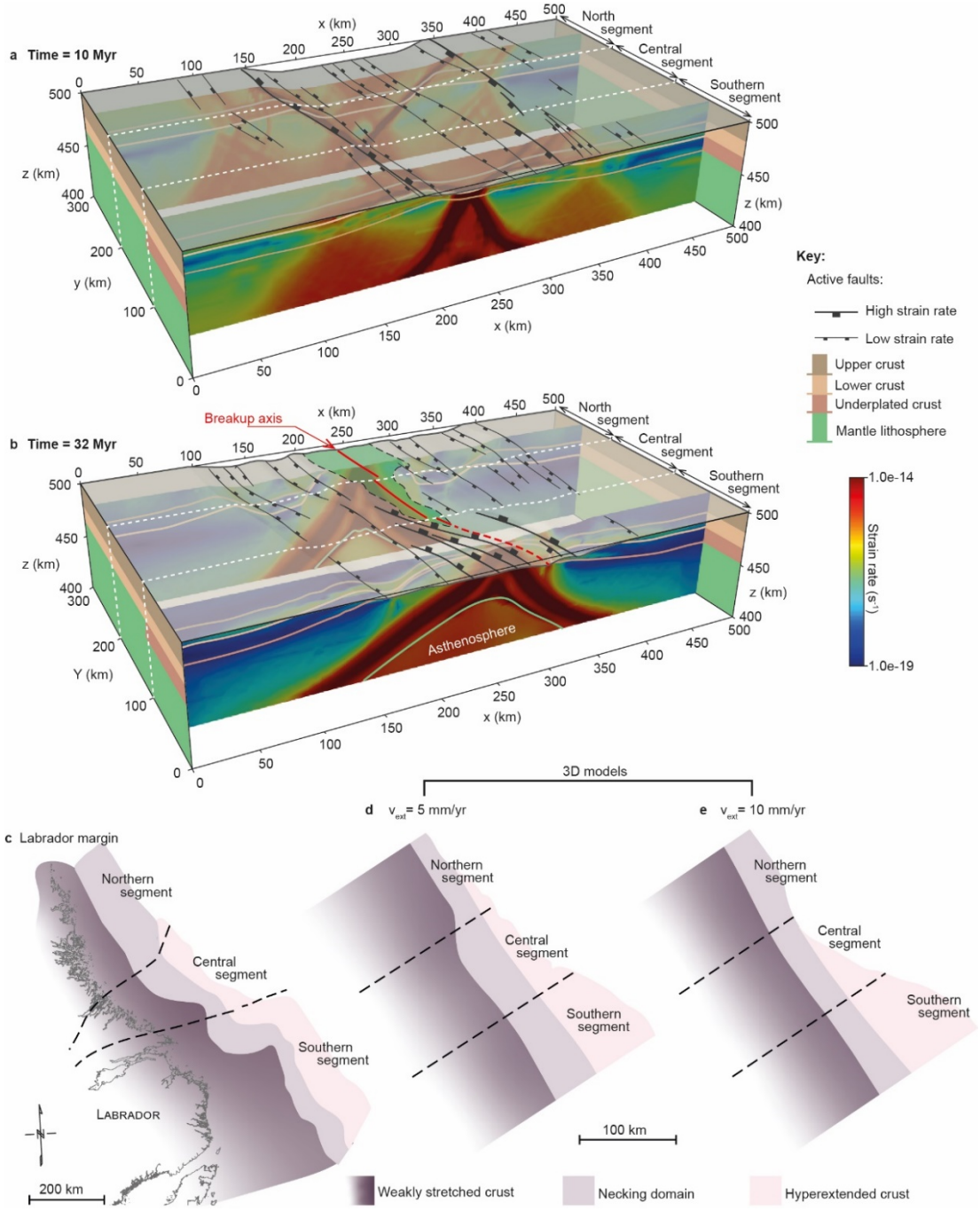

Fig. 4 | 3D modelling results. The 3D numerical experiment, at a slow extension rate (vext= 5 mm/yr), showing the distribution of active faults, which control rifting during the early stretching phase (a) and during the southward propagation of crustal breakup (b). Structural segmentation is evident early on in the rifling process, with faults ending or coalescing at segment boundaries (a). Crustal segmentation occurs shortly after the necking stage when the crust breaks in the north while hyperextension is taking place in the south (b). Once full crustal breakup is accomplished along the model, the obtained crustal architecture (d, e) appears segmented with a narrow margin in the north (no hyperextension) and a wide hyperextended crust in the south. This is comparable to the crustal architecture observed along the Labrador margin (c). The extension rate has minor effects on the final crustal geometry (d, e).

with observations from the Labrador Sea[26] (Fig. 4c-e) and illustrate the key role that lateral rheological heterogeneities have in promoting rifted margin segmentation.

Our geodynamic models emphasise the role of pre-rift lithospheric heterogeneities in defining rift evolution and crustal architecture along rifted margins. The results of the 2D experiments are consistent with previous numerical studies on the role of rheology in lithospheric extension[5,20], and demonstrate that the initial strength of the lower crust (i.e., composition and temperature), geothermal gradient, and the competition between frictional and viscous strain (i.e., decoupling) dictate the nature and timing of tectonic processes controlling lithospheric thinning. However, the 3D models with variable crustal rheology between the southern, central, and northern segments are unique and provide for the first time insights into how lateral rheological heterogeneities promote segmentation along rifted margins. The segmentation manifests laterally in the distribution of rift structures, the variability in crustal architecture, and the diachrony in breakup. It is not only expressed by a reactivation of pre-existing structures (e.g., sutures and shear zones), and is rather driven by the change in the processes controlling rifting within each segment.

Our findings are important to understand the evolution of rifted margins, which in most cases initiate on a lithosphere with strong inherited lateral heterogeneities. This is the case of the Labrador Sea, where variations in heat flow, lithospheric and crustal thickness and composition, are observed in the unstretched Canadian Shield. We demonstrate that observations from the margin hinterland could be used as a proxy for the initial (thermal and compositional) state of the lithosphere.

Methods

Governing Equations. We model the thermal-mechanical evolution of continental extension in a heterogenous initial lithosphere using the open-source and CIG-supported finite element code ASPECT version 2.0.1-pre[34,35]. The ASPECT version and parameter files required to reproduce our experiments can be found in the following GitHub branch:

https://github.com/naliboff/aspect/tree/labrador_sea_gouiza_naliboff_2020.

Velocity and pressure are solved for assuming incompressible viscous flow, where the Stokes equations are defined as:

$$\nabla \cdot u = 0$$

$$-\nabla \cdot 2\mu\dot{\varepsilon}(u) + \nabla P = \rho g$$

Above, $u$is velocity, $\mu$is viscosity, $\dot{\varepsilon}$is the deviatoric strain rate, $P$is pressure $\rho$is density and $g$is gravity.

Thermal evolution is modelled through the advection-diffusion equation:

$$\rho C_p \left(\frac{\partial T}{\partial t} + u \cdot \nabla T\right) - \nabla \cdot K \nabla T = \rho H$$

where $C_p$is the heat capacity, $T$is temperature, $t$is time, $K$is thermal conductivity and $H$is the rate of internal heating. Density varies linearly as a function of the reference density (ρ_0), thermal expansivity (α), reference temperature (T_0) and temperature:

$$\rho = \rho_0 \left(1 - \alpha(T - T_0)\right)$$

Rheological Formulation. The constitutive behaviour combines non-linear viscous flow with brittle failure (see Glerum et al. 2018 and Text S1 for further details), with viscous flow following a dislocation creep formulation:

$$\sigma'_{eff} = A^{-1/n} \dot{\varepsilon}_{eff}^{1/n} e^{\frac{Q+PV}{nRT}}$$

Above, σ'_{eff} is the effective stress (invariant), A is the viscous prefactor, n is the stress exponent, $\dot{\varepsilon}_{eff}$ is the second invariant of the deviatoric strain rate (effective strain rate), Q is the activation energy, P is pressure, V is the activation volume, T is temperature, and R is the gas constant.

Brittle (plastic) behaviour follows a Drucker-Prager yield criterion formulation, where the yield stress in 3D is a function of the cohesion (C), angle of internal friction (ϕ), and pressure (P):

$$\sigma'_{eff} = \frac{6Ccos(\phi) + 2Psin(\phi)}{\sqrt{(3)}(3 + sin(\phi))}$$

To help localize deformation and account for geologic observations of strain localization, we track the accumulation of plastic strain (invariant form) and weaken the cohesion and friction linearly by a factor of 2 or 4 between plastic strain values of 0.5 and 1.5[10,13].

The procedure for calculating the viscosity at every point follows the viscosity rescaling method, which

first compares the predicted effective stresses from viscous flow and plastic failure. If the viscous stress exceeds the plastic yield stress, the viscosity is reduced so the effective stress exactly matches the plastic yield stress[18,41].

Discretization and Nonlinear solvers. Throughout the model domain we use quadratic elements (Q2) elements to solve the advection-diffusion equation for temperature, while the Stokes equation is solved on elements that are quadratic for velocity and continuous linear for pressure (Q2Q1). The element size is 10 km beneath 300 km depth, 5 km from 100 to 200 km depth, and 2.5 km above 100 km depth. In total, the 3D numerical simulations contain ~463 million degrees of freedom. Compositional fields are used to track and advect distinct lithologic domains (e.g., rock types) and other time-dependent quantities (strain). The use of discontinuous Galerkin element with a limiter for compositional fields[42] minimizes diffusion of distinct layers and improves the accuracy of interface advection through time.

Nonlinearity introduced by the constitutive model is resolved using standard Picard iterations for the velocity and pressure to a tolerance of 10^{-4}. In most models we use a conservative maximum time step of 20,000 years to limit numerical instabilities during advection and improve the nonlinear convergence behaviour. This value is adjusted proportionally as the boundary velocity values increase or decrease. We use this outlined numerical approach to construct a series of 2D and 3D continental rifting simulations that reveal the relationship between initial lithospheric structure and rifted margin structure. In order to provide a robust sensitivity analysis of key modelling variables, we first carefully consider the geologic constraints on the pre-rift lithospheric structure.

References

1. Franke, D. Rifting, lithosphere breakup and volcanism: Comparison of magma-poor and volcanic rifted margins. *Mar. Pet. Geol.* **43**, 63–87 (2013).
2. Peron-Pinvidic, G., Manatschal, G. & Osmundsen, P. T. Structural comparison of archetypal Atlantic rifted margins: A review of observations and concepts. *Mar. Pet. Geol.* **43**, 21–47 (2013).
3. Buiter, S. J. H. & Torsvik, T. H. A review of Wilson Cycle plate margins: A role for mantle plumes in continental break-up along sutures? *Gondwana Res.* **26**, 627–653 (2014).
4. Lavier, L. L. & Manatschal, G. A mechanism to thin the continental lithosphere at magma-poor margins. *Nature* **440**, 324–328 (2006).
5. Huismans, R. & Beaumont, C. Depth-dependent extension, two-stage breakup and cratonic underplating at rifted margins. *Nature* **473**, 74–78 (2011).
6. Beaumont, C. & Ings, S. J. Effect of depleted continental lithosphere counterflow and inherited crustal weakness on rifting of the continental lithosphere: General results: RIFTING, COUNTERFLOW, AND OFFSET RIFTS. *J. Geophys. Res. Solid Earth* **117**, n/a-n/a (2012).
7. Brune, S., Heine, C., Pérez-Gussinyé, M. & Sobolev, S. V. Rift migration explains continental margin asymmetry and crustal hyper-extension. *Nat. Commun.* **5**, 4014 (2014).
8. Svartman Dias, A. E., Lavier, L. L. & Hayman, N. W. Conjugate rifted margins width and asymmetry: The interplay between lithospheric strength and thermomechanical processes. *J. Geophys. Res. Solid Earth* **120**, 8672–8700 (2015).
9. Tetreault, J. L. & Buiter, S. J. H. The influence of extension rate and crustal rheology on the evolution of passive margins from rifting to break-up. *Tectonophysics* **746**, 155–172 (2018).
10. Naliboff, J. & Buiter, S. J. H. Rift reactivation and migration during multiphase extension. *Earth Planet. Sci. Lett.* **421**, 58–67 (2015).
11. Jammes, S. & Lavier, L. L. The effect of bimineralic composition on extensional processes at lithospheric scale: RIFTING OF BIMINERALIC LITHOSPHERE. *Geochem. Geophys. Geosystems* **17**, 3375–3392 (2016).
12. Duretz, T. *et al.* The importance of structural softening for the evolution and architecture of passive margins. *Sci. Rep.* **6**, 38704 (2016).
13. Naliboff, J. B., Buiter, S. J. H., Péron-Pinvidic, G., Osmundsen, P. T. & Tetreault, J. Complex fault interaction controls continental rifting. *Nat. Commun.* **8**, 1179 (2017).
14. Liao, J. & Gerya, T. From continental rifting to seafloor spreading: Insight from 3D thermo-mechanical modeling. *Gondwana Res.* **28**, 1329–1343 (2015).
15. Le Pourhiet, L., May, D. A., Huille, L., Watremez, L. & Leroy, S. A genetic link between transform and hyper-extended margins. *Earth Planet. Sci. Lett.* **465**, 184–192 (2017).
16. Balázs, A., Matenco, L., Vogt, K., Cloetingh, S. & Gerya, T. Extensional Polarity Change in Continental Rifts: Inferences From 3-D Numerical Modeling and Observations. *J. Geophys. Res. Solid Earth* **123**, 8073–8094 (2018).
17. Heron, P. J. *et al.* Segmentation of Rifts Through Structural Inheritance: Creation of the Davis Strait. *Tectonics* **38**, 2411–2430 (2019).
18. Naliboff, J. B., Glerum, A., Brune, S., Péron-Pinvidic, G. & Wrona, T. Development of 3D rift heterogeneity through fault network evolution. *Geophys. Res. Lett.* **n/a**, e2019GL086611.
19. Le Pourhiet, L. *et al.* Continental break-up of the South China Sea stalled by far-field compression. *Nat. Geosci.* **11**, 605–609 (2018).
20. Brune, S. Evolution of stress and fault patterns in oblique rift systems: 3-D numerical lithospheric-scale experiments from rift to breakup. *Geochem. Geophys. Geosystems* **15**, 3392–3415 (2014).
21. Duclaux, G., Huismans, R. S. & May, D. A. Rotation, narrowing, and preferential reactivation of brittle structures during oblique rifting. *Earth Planet. Sci. Lett.* **531**, 115952 (2020).

22. Phillips, T. B., Jackson, C. A.-L., Bell, R. E., Duffy, O. B. & Fossen, H. Reactivation of intrabasement structures during rifting: A case study from offshore southern Norway. *J. Struct. Geol.* **91**, 54–73 (2016).
23. Shapiro, N. M., Ritzwoller, M. H., Mareschal, J. C. & Jaupart, C. Lithospheric structure of the Canadian Shield inferred from inversion of surface-wave dispersion with thermodynamic a priori constraints. *Geol. Soc. Lond. Spec. Publ.* **239**, 175–194 (2004).
24. Yuan, H. & Romanowicz, B. Lithospheric layering in the North American craton. *Nature* **466**, 1063–1068 (2010).
25. Welford, J. K. & Hall, J. Lithospheric structure of the Labrador Sea from constrained 3-D gravity inversion. *Geophys. J. Int.* **195**, 767–784 (2013).
26. Gouiza, M. & Paton, D. A. The Role of Inherited Lithospheric Heterogeneities in Defining the Crustal Architecture of Rifted Margins and the Magmatic Budget During Continental Breakup. *Geochem. Geophys. Geosystems* **20**, 1836–1853 (2019).
27. Dickie, K., Keen, C. E., Williams, G. L. & Dehler, S. A. Tectonostratigraphic evolution of the Labrador margin, Atlantic Canada. *Mar. Pet. Geol.* **28**, 1663–1675 (2011).
28. Keen, C. E., Dickie, K. & Dafoe, L. T. Structural Evolution of the Rifted Margin off Northern Labrador: The Role of Hyperextension and Magmatism. *Tectonics* **37**, 1955–1972 (2018).
29. Keen, C. E., Dickie, K. & Dafoe, L. T. Structural characteristics of the ocean-continent transition along the rifted continental margin, offshore central Labrador. *Mar. Pet. Geol.* **89**, 443–463 (2018).
30. Srivastava, S. P. & Roest, W. R. Extent of oceanic crust in the Labrador Sea. *Mar. Pet. Geol.* **16**, 65–84 (1999).
31. Steinberger, B., Bredow, E., Lebedev, S., Schaeffer, A. & Torsvik, T. H. Widespread volcanism in the Greenland–North Atlantic region explained by the Iceland plume. *Nat. Geosci.* **12**, 61 (2019).
32. Funck, T., Louden, K. E. & Reid, I. D. Crustal structure of the Grenville Province in southeastern Labrador from refraction seismic data: evidence for a high-velocity lower crustal wedge. *Can. J. Earth Sci.* **38**, 1463–1478 (2001).
33. Mareschal, J. C. & Jaupart, C. Variations of surface heat flow and lithospheric thermal structure beneath the North American craton. *Earth Planet. Sci. Lett.* **223**, 65–77 (2004).
34. Kronbichler, M., Heister, T. & Bangerth, W. High accuracy mantle convection simulation through modern numerical methods: High accuracy mantle convection simulation. *Geophys. J. Int.* **191**, 12–29 (2012).
35. Heister, T., Dannberg, J., Gassmöller, R. & Bangerth, W. High accuracy mantle convection simulation through modern numerical methods – II: realistic models and problems. *Geophys. J. Int.* **210**, 833–851 (2017).
36. Rutter, E. H. & Brodie, K. H. Experimental grain size-sensitive flow of hot-pressed Brazilian quartz aggregates. *J. Struct. Geol.* **26**, 2011–2023 (2004).
37. Rybacki, E., Gottschalk, M., Wirth, R. & Dresen, G. Influence of water fugacity and activation volume on the flow properties of fine-grained anorthite aggregates. *J. Geophys. Res. Solid Earth* **111**, B03203 (2006).
38. Gleason, G. C. & Tullis, J. A flow law for dislocation creep of quartz aggregates determined with the molten salt cell. *Tectonophysics* **247**, 1–23 (1995).
39. Vauchez, A., Tommasi, A. & Barruol, G. Rheological heterogeneity, mechanical anisotropy and deformation of the continental lithosphere. *Tectonophysics* **296**, 61–86 (1998).
40. Mareschal, J.-C. & Jaupart, C. Radiogenic heat production, thermal regime and evolution of continental crust. *Tectonophysics* **609**, 524–534 (2013).
41. Glerum, A., Thieulot, C., Fraters, M., Blom, C. & Spakman, W. Nonlinear viscoplasticity in ASPECT: benchmarking and applications to subduction. *Solid Earth* **9**, 267–294 (2018).
42. He, Y., Puckett, E. G. & Billen, M. I. A discontinuous Galerkin method with a bound preserving limiter for the advection of non-diffusive fields in solid Earth geodynamics. *Phys. Earth Planet. Inter.* **263**, 23–37 (2017).

Acknowledgements

We thank the Computational Infrastructure for Geodynamics (geodynamics.org) which is funded by the National Science Foundation under award EAR-0949446 and EAR-1550901 for supporting the development of ASPECT.

The 2D modelling was undertaken on ARC4, part of the High Performance Computing facilities at the University of Leeds, UK. The computational time for the 3D simulations was provided under XSEDE project EAR180001. Data Availability Statement Following the FAIR data practices and guidelines, the version of ASPECT and parameter files required to reproduce our experiments are available on GitHub at https://github.com/naliboff/aspect under the branch labrador_sea_gouiza_naliboff_2020. ASPECT is built on the open-source finite element package deal. II, which we built (version 9.0.0) through the candi installation package (https://github.com/dealii/candi). Additional dependencies built through candi include Trilinos (12.10.1) and p4est (2.0.0). Detailed instructions for building ASPECT and deal. II on the XSEDE-supported supercomputer Stampede2 are available at https://github.com/geodynamics/aspect/wiki. The work described in this paper was primarily funded through the Basin Structure Group (BSG, University of Leeds) and by the Computational Infrastructure for Geodynamics (NSF award 1550901).

Author contributions

M.G. conceived the original idea for the investigation, co-designed and tested the numerical simulations, analysed and visualized the simulations, and co-wrote the publication. J.N. co-designed and tested the numerical simulations and co-wrote the publication.

Additional information

Supplementary Information accompanies this preprint.

Competing interests: The authors declare no competing interests.

Supplementary information to

Rheological inheritance controls the formation of segmented rifted margins in cratonic lithosphere

M. Gouiza[1]* and J. Naliboff[2,3]
[1] School of Earth and Environment, University of Leeds, Leeds, UK.
[2] Department of Earth and Planetary Sciences, University of California, Davis, USA.
[3] New Mexico Institute of Mining and Technology, Socorro, New Mexico, USA.

Note 1: Extension rates, continental breakup, and seafloor spreading in the Labrador Sea

Extension rates were calculated along seismic sections from the Labrador margin using crustal thickness estimates[1]. We assume an initial crustal thickness of 50 km in the southern segment and 35 km in the central and northern segments, and an extension duration of 65 Myr (ca. 145-80 Ma). For the central and southern segments, mantle exhumation was accounted for by calculating exhumation rates as the length of the exhumed mantle divided by the duration of exhumation, estimated at 15 Myr (ca. 80-65 Ma).

Continental extension occurred during the Cretaceous (ca. 145-80 Ma) and was very slow in the north (ca. 1 mm/yr) and increased southwards, where extension rates of ca. 1.1 to 2.1 mm/yr and 2.2 to 3.7 mm/yr are recorded in the central and southern segments, respectively (Supplementary Table 2). Mantle exhumation, documented only in the COT of the central and southern segments of the Labrador margin, took place during ca. 15 Myr (ca. 80-65 Ma) at much higher rates of 4.2 to 5.2 mm/yr and 5.3 to 8.7 mm/yr, respectively (Supplementary Table 2).

The present-day crustal architecture, depicted by seismic data and gravity modelling, suggest an asymmetric rifting in the Labrador Sea, which displays wider shelf and necking domains on the Canadian side than on the Greenland side[1–3]. Ref. [4] suggests that the line of breakup was closer to the Greenland side (i.e., upper plate) than the Labrador side (i.e., lower plate), which means that most the syn-rift stretching is preserved on the Canadian side of the basin. Overall, stretching in the Labrador Sea appears to be characterized by slow crustal extension rates then higher mantle exhumation rates.

Various ages of continental breakup were proposed in the Labrador Sea, ranging from Turonian (ca. 92 Ma), based on a stratigraphic unconformity[5], to Palaeocene (ca. 62 Ma), corresponding to the magnetic anomalies of Chron 27[6]. Ref. [1] used seismic reflection lines (to identify the extent of oceanic crust) combined with magnetic chrons[7] to propose a diachronous continental breakup younging northward. They suggest that oceanic accretion started ca. 65.8-64.4 Ma in the south (i.e., Chron 29), ca. 63.3-61.1 Ma in the centre (i.e., between Chron 29 and Chron 27), and ca. 60.5-57.7 Ma in the north (i.e., Chron 26). The latter coincides with the mid to late Palaeocene (ca. 61-56 Ma) flood basalts, which are found around the Davis Strait and attributed to the Iceland plume[8,9].

Seafloor spreading in the Labrador Sea experienced a change in direction from NE-SW to N-S at ca. 60 Ma[10]. Then at ca. 50 Ma spreading rate decreased from 10 to 3-4 mm/yr (half spreading rates) before it completely ceased at the Eocene-Oligocene boundary[10] (ca. 34 Ma).

Note 2: Surface heat flow onshore the Labrador margin

Data from the east Canadian Shield, onshore the Labrador margin. show a noticeable southward increase in surface heat flow[11]. Surface heat flow values range between ca. 22-27 mW/m^2 in the Churchill and Nain provinces in the north, 27-37 mW/m^2 in the Makkovik province in the centre, and 27-47 mW/m^2 in the Grenville province in the south. Variations in heat flow can be explained by changes in crustal radiogenic heat production (i.e., differences in crustal thickness and/or composition), while regional-scale variations are related to changes in lithospheric mantle heat flow[12,13].

The southward increase in surface heat flow onshore Labrador is consistent with the observed increase and decrease in crustal and lithospheric thickness south of the Grenville Front, respectively. Lateral variations in shear velocities across the Grenville Front at depths ranging between 80 and 150 km also suggests changes in temperature (and composition) of the deep mantle lithosphere[14]. The Grenville Front was a major suture zone along which the Superior province was subducted toward the SE underneath the Grenville province, giving rise to calc-alkaline arcs[15] (ca. 1.68 to 1.66 Ga). This magmatism has resulted in the depletion of the mantle underneath the Grenville domain, such as attested by the distribution of post subduction magmatism which is found on both sides of the Labrador Sea but mostly north of the Grenville Front[16].

Note 3: Initial thermal structure of the numerical experiments

Each of the three segments of the Labrador Sea is represented by a distinct lithospheric structure setup, which is constrained by observations from the Labrador Sea and the Canadian Shield[1] with fixed initial model geometry, temperature structure, mantle rheology, and extension rate (Fig. 2).

The model setup for the north segment has a 200 km thick pre-rift lithosphere with a 20 km thick upper crust and a 15 km thick lower crust. The model setup for the central segment has a 175 km thick pre-rift lithosphere with a 20 km thick upper crust and a 15 km thick lower crust. The model setup for the south segment has a 150 km thick pre-rift lithosphere with a 20 km thick upper crust, a 15 km thick lower crust, and a 15 km thick underplated high density crust.

We assume a weak (fertile) mantle in the north and central segments. which is governed by wet olivine flow low[17], while in the southern segment we use a strong (depleted) mantle lithosphere defined by dry olivine flow law and a weak (fertile) asthenosphere defined by wet olivine flow law[17].

The initial thermal structure of each model is calculated using the following thermal gradient equation[12]:

$$T(z) = T_t + \left(\frac{q_t}{k}\right) z - \frac{(A\ z^2)}{(2\ k)} q_t = q_b + (A\ \Delta z)$$

where T(z) is the temperature at a given depth (z), T_t is temperature at the top of the layer, q_t is the heat flow at the top of the layer, q_b is the heat flow at the base of the layer, A is the radiogenic heat production of the layer, k is the thermal conductivity of the layer, and Δz is the thickness of the layer.

We use surface heat flow of 25, 32.5, and 40 mW/m^2 for the northern, central, and southern segments respectively, constant radiogenic heat production in the mantle lithosphere (0.01 μW/m^3) and lower crust (0.04 μW/m^3 if felsic and 0.02 μW/m^3 if mafic), and constant temperature at the lithosphere-asthenosphere boundary (1330 °C). The calculated thermal profiles are shown in Figure 2 and the full thermal parameters are given in Supplementary Table 2.

Supplementary Table 1: Extension rates calculated in the Labrador margin along seismic lines[1] assuming area conservation in 2D. t_{ext}: duration of crustal extension; l_f: final (present-day) length of continental crust along the seismic line; a: continental crust area defined by top basement and Moho; $l_i = a/d_i$ where l_i is the initial (pre-rift) length of continental crust and d_i is the initial (pre-rift) crust thickness (35 km in the northern and central segments, 50 km in the southern segment); $v_{ext} = (l_f - l_i)/t_{ext}$ is the extension rate; t_{exh}: duration of mantle exhumation; l_m: length of exhumed mantle domain along seismic lines; $v_{exh} = l_m/t_{exh}$ is the exhumation rate. Seismic lines are listed from north to south respectively.

	Lines	Continental crust extension						Mantle exhumation				Total extension rate (mm/yr)	
		t_{ext} (Myr)	l_f (km)	a (km^2)	l_i (km)	v_{ext} (mm/yr)		t_{exh} (Myr)	l_m	v_{exh} (mm/yr)			
Northern segment	1	65	92	1036	30	**1.0**	**1.0**	No mantle exhumation				**1.0**	
	2		92	1020	29	**1.0**							
Central segment	3		107	1133	32	**1.1**	**1.6**	15	57	**3.8**	**4.5**	**1.6**	**2.1**
	4		170	1264	36	**2.1**			78	**5.2**		**2.6**	
Southern segment	5		272	2935	59	**3.3**	**3**		110	**7.3**	**7.0**	**4.0**	**3.7**
	6		298	4439	89	**3.2**			108	**7.2**		**4.0**	
	7		349	4562	91	**4.0**			90	**6.0**		**4.3**	
	8		168	1267	25	**2.2**			85	**5.7**		**3**	
	10		196	2478	50	**2.3**			131	**8.7**		**3.5**	

Supplementary Table 2: Thermo-mechanical parameters used for the numerical modelling**.**

Parameters			Upper crust	Lower crust	Underplated crust	Mantle lithosphere	Asthenosphere
Density (kg/m$^{3)}$			2700	2850	3000	3250	3300
Radiogenic heat production (μW m^{-3})	*Northern segment*		0.202e-6	0.04e-6 (if wet quartzite flow law) 0.02e-6 (if wet anorthite flow law)	-	0.01e-6	0
	Central segment		0.457e-6		-		
	Southern segment		0.662e-6		0.02e-4		
Thermal conductivity (W K^{-1} m^{-1})			3				0
Thermal diffusivity (m^2 s^{-1})			1.428571e-6	1.403508e-6	1.333333e-6	1.230769e-6	1.212121e-6
Heat Capacity (J kg^{-1} K^{-1})			750				
Thermal expansivity (K^{-1})			2e5				
Angle of internal friction (°)			30				
Cohesion (MPa)			20e6				
Strain weakening interval			0.5 - 1.5				
Strain weakening factor			0.25				
Wet quartzite[18]	*Prefactor*		8.57e-28		-		
	Stress exponent		4		-		
	Activation energy (J mol^{-1})		223e3		-		
Wet anorthite[19]	*Prefactor*			7.13e-18		-	
	Stress exponent			3		-	
	Activation energy (J mol^{-1})			345		-	
Dry olivine[17]	*Prefactor*	*Dislocation*	-			6.52e-16	-
		Diffusion	-			2.37e-15	-
	Stress exponent	*Dislocation*	-			3.5	-
		Diffusion	-			1	-
	Activation energy (J mol^{-1})	*Dislocation*	-			530e3	-
		Diffusion	-			375e3	-
	Activation	*Dislocation*	-			18e-6	-

	volume (m^3 mol^{-1})	*Diffusion*	-	10e-6	-
Wet olivine[17]	*Prefactor*	*Dislocation*	-	5.33e-19	
		Diffusion	-	1.50e-18	
	Stress exponent	*Dislocation*	-	3.5	
		Diffusion	-	1	
	Activation energy (J mol^{-1})	*Dislocation*	-	480e3	
		Diffusion	-	335e3	
	Activation volume (m^3 mol^{-1})	*Dislocation*	-	11e-6	
		Diffusion	-	4e-6	

All the supplementary videos can be viewed and downloaded from here: http://dx.doi.org/10.17632/9h3vjvn2ms.1

Supplementary Video 1: Northern segment, slow extension, weak lower crust

2D numerical model of the northern segment assuming wet quartzite flow law in the upper and lower crust, wet olivine flow law in the mantle, and an extension rate of 5 mm/yr. The upper panel shows the strain rate. The lower left panel shows the distribution of plastic/brittle and viscous/ductile layers. The lower right panel shows the density. Isotherm curves are shown in all three panels.

Supplementary Video 2: Central segment, slow extension, weak lower crust

2D numerical model of the central segment assuming wet quartzite flow law in the upper and lower crust, wet olivine flow law in the mantle, and an extension rate of 5 mm/yr. The upper panel shows the strain rate. The lower left panel shows the distribution of plastic/brittle and viscous/ductile layers. The lower right panel shows the density. Isotherm curves are shown in all three panels.

Supplementary Video 3: Southern segment, slow extension, weak lower crust

2D numerical model of the southern segment assuming wet quartzite flow law in the upper and lower crust, an anorthite flow law in the underplated crust, dry olivine flow law in the mantle lithosphere, wet olivine flow law in the asthenosphere, and an extension rate of 5 mm/yr. The upper panel shows the strain rate. The lower left panel shows the distribution of plastic/brittle and viscous/ductile layers. The lower right panel shows the density. Isotherm curves are shown in all three panels.

Supplementary Video 4: Northern segment, slow extension, strong lower crust

2D numerical model of the northern segment assuming wet quartzite flow law in the upper crust, wet anorthite flow law in the lower crust, wet olivine flow law in the mantle, and an extension rate of 5 mm/yr. The upper panel shows the strain rate. The lower left panel shows the distribution of plastic/brittle and viscous/ductile layers. The lower right panel shows the density. Isotherm curves are shown in all three panels.

Supplementary Video 5: Central segment, slow extension, strong lower crust

2D numerical model of the central segment assuming wet quartzite flow law in the upper crust, wet anorthite flow law in the lower crust, wet olivine flow law in the mantle, and an extension rate of 5 mm/yr. The upper panel shows the strain rate. The lower left panel shows the distribution of plastic/brittle and viscous/ductile layers. The lower right panel shows the density. Isotherm curves are shown in all three panels.

Supplementary Video 6: Southern segment, Slow extension, strong lower crust

2D numerical model of the southern segment assuming a wet quartzite flow law in the upper crust, anorthite flow law in the lower crust and underplated crust, dry olivine flow law in the mantle lithosphere, wet olivine flow law in the asthenosphere, and an extension rate of 5 mm/yr. The upper panel shows the strain rate. The lower left panel shows the distribution of plastic/brittle and viscous/ductile layers. The lower right panel shows the density. Isotherm curves are shown in all three panels.

Supplementary Video 7: Northern segment, fast extension, weak lower crust

2D numerical model of the northern segment assuming wet quartzite flow law in the upper and lower crust, wet olivine flow law in the mantle, and an extension rate of 10 mm/yr. The upper panel shows the strain rate. The lower left panel

shows the distribution of plastic/brittle and viscous/ductile layers. The lower right panel shows the density. Isotherm curves are shown in all three panels.

Supplementary Video 8: Central segment, fast extension, weak lower crust

2D numerical model of the central segment assuming wet quartzite flow law in the upper and lower crust, wet olivine flow law in the mantle, and an extension rate of 10 mm/yr. The upper panel shows the strain rate. The lower left panel shows the distribution of plastic/brittle and viscous/ductile layers. The lower right panel shows the density. Isotherm curves are shown in all three panels.

Supplementary Video 9: Southern segment, fast extension, weak lower crust

2D numerical model of the southern segment assuming wet quartzite flow law in the upper and lower crust, an anorthite flow law in the underplated crust, dry olivine flow law in the mantle lithosphere, wet olivine flow law in the asthenosphere, and an extension rate of 10 mm/yr. The upper panel shows the strain rate. The lower left panel shows the distribution of plastic/brittle and viscous/ductile layers. The lower right panel shows the density. Isotherm curves are shown in all three panels.

Supplementary Video 10: Northern segment, fast extension, strong lower crust

2D numerical model of the northern segment assuming wet quartzite flow law in the upper crust, wet anorthite flow law in the lower crust, wet olivine flow law in the mantle, and an extension rate of 10 mm/yr. The upper panel shows the strain rate. The lower left panel shows the distribution of plastic/brittle and viscous/ductile layers. The lower right panel shows the density. Isotherm curves are shown in all three panels.

Supplementary Video 11: Central segment, fast extension, strong lower crust

2D numerical model of the central segment assuming wet quartzite flow law in the upper crust, wet anorthite flow law in the lower crust, wet olivine flow law in the mantle, and an extension rate of 10 mm/yr. The upper panel shows the strain rate. The lower left panel shows the distribution of plastic/brittle and viscous/ductile layers. The lower right panel shows the density. Isotherm curves are shown in all three panels.

Supplementary Video 12: Southern segment, fast extension, strong lower crust

2D numerical model of the southern segment assuming a wet quartzite flow law in the upper crust, anorthite flow law in the lower crust and underplated crust, dry olivine flow law in the mantle lithosphere, wet olivine flow law in the asthenosphere, and an extension rate of 10 mm/yr. The upper panel shows the strain rate. The lower left panel shows the distribution of plastic/brittle and viscous/ductile layers. The lower right panel shows the density. Isotherm curves are shown in all three panels.

Supplementary Video 13: 3D model, slow extension, weak lower crust

3D numerical model with the same constant boundary conditions as the 2D models of the three segments (Fig. 2). Here use a weak wet quartzite flow law in the lower crust and an extension rate of 5 mm/yr. The upper panel shows the evolution of the 3D model coloured by density. The lower left and right panels show strain rate coloured slices, with isotherms, through the northern and southern segments, respectively.

Supplementary Video 14: 3D model, slow extension, strong lower crust

3D numerical model with the same constant boundary conditions as the 2D models of the three segments (Fig. 2). Here use a strong wet anorthite flow law in the lower crust and an extension rate of 5 mm/yr. The upper panel shows the evolution of the 3D model coloured by density. The lower left and right panels show strain rate coloured slices, with isotherms, through the northern and southern segments, respectively.

Supplementary Video 15: 3D model, fast extension, weak lower crust

3D numerical model with the same constant boundary conditions as the 2D models of the three segments (Fig. 2). Here use a weak wet quartzite flow law in the lower crust and an extension rate of 10 mm/yr. The upper panel shows the evolution of the 3D model coloured by density. The lower left and right panels show strain rate coloured slices, with isotherms, through the northern and southern segments, respectively.

Supplementary Video 16: 3D model, fast extension, strong lower crust

3D numerical model with the same constant boundary conditions as the 2D models of the three segments (Fig. 2). Here use a strong wet anorthite flow law in the lower crust and an extension rate of 10 mm/yr. The upper panel shows the evolution of the 3D model coloured by density. The lower left and right panels show strain rate coloured slices, with isotherms, through the northern and southern segments, respectively.

Supplementary Video 17: 3D model, slow extension, variable rheology

3D numerical model with the same constant boundary conditions as the 2D models of the three segments (Fig. 2). The lower crust is governed by the strong wet anorthite flow law in the north and the weak wet quartzite flow law in the centre and the south. The extension rate is 5 mm/yr. The upper panel shows the evolution of the 3D model coloured by density. The lower left and right panels show strain rate coloured slices, with isotherms, through the northern and southern segments, respectively.

Supplementary Video 18: 3D model, fast extension, variable rheology

3D numerical model with the same constant boundary conditions as the 2D models of the three segments (Fig. 2). The lower crust is governed by the strong wet anorthite flow law in the north and the weak wet quartzite flow law in the centre and the south. The extension rate is 10 mm/yr. The upper panel shows the evolution of the 3D model coloured by density. The lower left and right panels show strain rate coloured slices, with isotherms, through the northern and southern segments, respectively.

Supplementary references

1. Gouiza, M. & Paton, D. A. The Role of Inherited Lithospheric Heterogeneities in Defining the Crustal Architecture of Rifted Margins and the Magmatic Budget During Continental Breakup. *Geochem. Geophys. Geosystems* **20**, 1836–1853 (2019).
2. Chian, D., Louden, K. E. & Reid, I. Crustal structure of the Labrador Sea conjugate margin and implications for the formation of nonvolcanic continental margins. *J. Geophys. Res. Solid Earth* **100**, 24239–24253 (1995).
3. Welford, J. K. & Hall, J. Lithospheric structure of the Labrador Sea from constrained 3-D gravity inversion. *Geophys. J. Int.* **195**, 767–784 (2013).
4. Peace, A. *et al.* An evaluation of Mesozoic rift-related magmatism on the margins of the Labrador Sea: Implications for rifting and passive margin asymmetry. *Geosphere* **12**, 1701–1724 (2016).
5. Balkwill, H. R. & McMillan, N. J. Mesozoic - Cenozoic geology of the Labrador shelf. in *Geology of the Continental Margin of Eastern Canada, Geology of Canada* (eds. Keen, M. J. & Williams, G. L.) vol. 2 31–85 (1990).
6. Chalmers, J. A. & Laursen, K. H. Labrador Sea: the extent of continental and oceanic crust and the timing of the onset of seafloor spreading. *Mar. Pet. Geol.* **12**, 205–217 (1995).
7. Srivastava, S. P. & Roest, W. R. Extent of oceanic crust in the Labrador Sea. *Mar. Pet. Geol.* **16**, 65–84 (1999).
8. Steinberger, B., Bredow, E., Lebedev, S., Schaeffer, A. & Torsvik, T. H. Widespread volcanism in the Greenland–North Atlantic region explained by the Iceland plume. *Nat. Geosci.* **12**, 61 (2019).
9. Storey, M., Duncan, R. A. & Tegner, C. Timing and duration of volcanism in the North Atlantic Igneous Province: Implications for geodynamics and links to the Iceland hotspot. *Chem. Geol.* **241**, 264–281 (2007).
10. Roest, W. R. & Srivastava, S. P. Sea-floor spreading in the Labrador Sea: A new reconstruction. *Geology* **17**, 1000–1003 (1989).
11. Mareschal, J. C. & Jaupart, C. Variations of surface heat flow and lithospheric thermal structure beneath the North American craton. *Earth Planet. Sci. Lett.* **223**, 65–77 (2004).
12. Chapman, D. S. Thermal gradients in the continental crust. *Geol. Soc. Lond. Spec. Publ.* **24**, 63–70 (1986).
13. Mareschal, J.-C. & Jaupart, C. Radiogenic heat production, thermal regime and evolution of continental crust. *Tectonophysics* **609**, 524–534 (2013).
14. Shapiro, N. M., Ritzwoller, M. H., Mareschal, J. C. & Jaupart, C. Lithospheric structure of the Canadian Shield inferred from inversion of surface-wave dispersion with thermodynamic a priori constraints. *Geol. Soc. Lond. Spec. Publ.* **239**, 175–194 (2004).
15. Gower, C. F. The evolution of the Grenville Province in eastern Labrador, Canada. *Geol. Soc. Lond. Spec. Publ.* **112**, 197–218 (1996).
16. Tappe, S. *et al.* Craton reactivation on the Labrador Sea margins: 40Ar/39Ar age and Sr–Nd–Hf–Pb isotope constraints from alkaline and carbonatite intrusives. *Earth Planet. Sci. Lett.* **256**, 433–454 (2007).
17. Hirth, G. & Kohlstedt, D. Rheology of the upper mantle and the mantle wedge: A view from the experimentalists. in *Geophysical Monograph Series* (ed. Eiler, J.) vol. 138 83–105 (American Geophysical Union, 2003).
18. Rutter, E. H. & Brodie, K. H. Experimental grain size-sensitive flow of hot-pressed Brazilian quartz aggregates. *J. Struct. Geol.* **26**, 2011–2023 (2004).
19. Rybacki, E., Gottschalk, M., Wirth, R. & Dresen, G. Influence of water fugacity and activation volume on the flow properties of fine-grained anorthite aggregates. *J. Geophys. Res. Solid Earth* **111**, B03203 (2006).